The Effects of Doping Density and Temperature on the Optoelectronic Properties of Formamidinium Tin Triiodide Thin Films

Rebecca L. Milot, Matthew T. Klug, Christopher L. Davies, Zhiping Wang, Hans Kraus, Henry J. Snaith, Michael B. Johnston, and Laura M. Herz*

Optoelectronic properties are unraveled for formamidinium tin triiodide (FASnI$_3$) thin films, whose background hole doping density is varied through SnF$_2$ addition during film fabrication. Monomolecular charge-carrier recombination exhibits both a dopant-mediated part that grows linearly with hole doping density and remnant contributions that remain under tin-enriched processing conditions. At hole densities near 10^{20} cm^{-3}, a strong Burstein–Moss effect increases absorption onset energies by ≈300 meV beyond the bandgap energy of undoped FASnI$_3$ (shown to be 1.2 eV at 5 K and 1.35 eV at room temperature). At very high doping densities (10^{20} cm^{-3}), temperature-dependent measurements indicate that the effective charge-carrier mobility is suppressed through scattering with ionized dopants. Once the background hole concentration is nearer 10^{19} cm^{-3} and below, the charge-carrier mobility increases with decreasing temperature according to ≈$T^{-1.2}$, suggesting that it is limited mostly by intrinsic interactions with lattice vibrations. For the lowest doping concentration of 7.2×10^{18} cm^{-3}, charge-carrier mobilities reach a value of 67 cm^2 V^{-1} s^{-1} at room temperature and 470 cm^2 V^{-1} s^{-1} at 50 K. Intraexcitonic transitions observed in the THz-frequency photoconductivity spectra at 5 K reveal an exciton binding energy of only 3.1 meV for FASnI$_3$, in agreement with the low bandgap energy exhibited by this perovskite.

Hybrid metal halide perovskite semiconductors show great promise for application in optoelectronic devices[1–6] owing to a combination of facile synthesis from simple starting materials and remarkable optoelectronic properties for polycrystalline thin film materials.[1,7–9] Photovoltaic devices based on hybrid metal halide perovskites have been particularly impressive, with power conversion efficiencies (PCEs) now exceeding 22% and rivaling industry-standard devices fabricated with silicon active layers.[4] However, one potential drawback of hybrid perovskites is that the highest performing devices are currently based around lead-containing materials such as methylammonium lead triiodide (CH$_3$NH$_3$PbI$_3$ or MAPbI$_3$) or formamidinium lead triiodide (HC(NH$_2$)$_2$PbI$_3$ or FAPbI$_3$).[1] Lead and its compounds are known to be severely toxic even in small amounts and can cause both acute and chronic damage to all major organs and tissues,[10,11] as a result of which regulations tightly restrict its use in the majority

of consumer industries worldwide.[11] Although some applications including photovoltaics are exempt from certain regulations such as the European Union RoHS directives, most actively aim to limit the use of lead.[11,12] To address this concern, many alternative lead-free perovskites have been proposed, including direct analogs for which Pb^{2+} is substituted with a divalent cation, vacancy-ordered perovskites of the form A$_2$BM$_6$ where Pb^{2+} is replaced by a tetravalent metal cation, and double perovskites of the form A$_2$BB'M$_6$ where Pb^{2+} is substituted by either two divalent cations or the combination of a monovalent and a trivalent cation.[13–15] Although the chemical space for these substitutions is seemingly large, the requirements for strong visible absorption, high charge-carrier mobility, and low toxicity severely limit the number of realistic possibilities.[13,16–18] Computational screening of hundreds of perovskite materials have identified tin(II) perovskites of the form ASnX$_3$ as one of the more promising lead-free options.[16,17] In principle, tin perovskites have the potential to outperform analogous lead-based materials, as they are capable of achieving higher charge-carrier mobilities and exhibit bandgaps that are better matched to the solar spectrum for

Dr. R. L. Milot, Dr. M. T. Klug, C. L. Davies, Dr. Z. Wang,
Prof. H. J. Snaith, Prof. M. B. Johnston, Prof. L. M. Herz
Department of Physics
University of Oxford
Clarendon Laboratory
Parks Road, Oxford OX1 3PU, UK
E-mail: laura.herz@physics.ox.ac.uk
Dr. R. L. Milot
Department of Physics
University of Warwick
Gibbet Hill Road, Coventry CV4 7AL, UK
Prof. H. Kraus
Department of Physics
University of Oxford
Denys Wilkinson Building
Keble Road, Oxford OX1 3RH, UK

**ADVANCED
SCIENCE NEWS**

www.advancedsciencenews.com

**ADVANCED
MATERIALS**

www.advmat.de

maximum PCE of a single-junction.[7,14] Furthermore, tin(II) has fewer commercial restrictions, and tin perovskites are thought to be much less toxic, although studies on long-term health effects and toxicity of their degradation products are still ongoing.[10]

Despite these apparent advantages, the performance of tin-based perovskites still lags significantly behind that of their lead-containing counterparts. Photovoltaic device PCEs achieved with lead-free tin perovskites have reached values of only up to 9%,[14,19,20] which is superior to PCEs of most other reported lead-free options but is still well below 22% reported for lead-based materials.[4,13,15,21] The main reason for such lowered performance is that tin-based perovskites can easily become heavily p-doped as a result of tin vacancy formation during synthesis[14,22] or later degradation processes.[23] As a result, charge-carrier lifetimes are found to be lower[24–30] than for lead-based perovskites, leading to increased recombination losses, shortened charge-carrier diffusion lengths, and dramatically decreased device performance.[14]

One remedy to enhance the performance of tin perovskites solar cells has been to synthesize the thin films either under reducing conditions or with excess Sn^{2+}, which is usually in the form of SnF_2.[27–29,31–34] However, the exact origin of these increased efficiencies remains unclear as the presence of SnF_2 has been shown to change many aspects of the material.[35] For example, transient photoluminescence (PL) measurements have shown that SnF_2 treatment increased the monomolecular charge-carrier lifetime of tin perovskites,[27–29] likely because it lowers the probability of tin vacancy formation and the resulting background hole density.[14] However, SnF_2 addition has also been shown to change the energetics of the material,[36] provide increased stability,[31,33] and improve the film morphology.[29,32] Not all of the effects of SnF_2 addition are beneficial. For example, the addition of SnF_2 at higher concentrations can result in decreased device performance when SnF_2 aggregates form in the film.[19,33,34] As a result, many factors could ultimately influence the performance of solar cells made with SnF_2-treated tin perovskites,[35] and hence controlled doping studies of tin perovskite films are needed to analyze the full effects of these treatments on the optoelectronic parameters that govern light absorption and charge extraction. In addition, the complex interplay of extrinsic (doping) and intrinsic effects means that basic knowledge of the fundamental properties of these materials, such as exciton binding energies and mechanisms underpinning charge-carrier mobilities, are still outstanding.

Here, we conclusively unravel links between the hole doping density and the fundamental light-harvesting, change-generation, and transport properties of $FASnI_3$. Using noncontact, terahertz-frequency probes, we are able to determine accurately the hole background densities in $FASnI_3$ thin films, which we control by adding SnF_2 in varying amounts prior to film formation. We show that monomolecular dopant-mediated charge-carrier recombination rates vary linearly with doping density between 10^{18}–10^{20} cm^{-3} and find that sizeable trap-mediated recombination remains even in the limit of zero hole doping, pointing toward the need for alternative strategies to decrease trap density. Temperature-dependent absorption spectra reveal large Burstein–Moss shifts of several hundred meV for doping

densities above 10^{20} cm^{-3}. These shifts mask the true bandgap energy, which we determine through extrapolation of the absorption onset determined as a function of doping density. Although such shifts allow for convenient tuning of the absorption characteristics, they also lead to sizeable Stokes shifts between absorption and emission that will induce open-circuit voltage losses in photovoltaic devices. In addition, we examine the mechanisms that determine charge-carrier mobility through an investigation of its temperature-dependence. We find that for doping densities above 10^{20} cm^{-3}, the effective charge-carrier mobility in $FASnI_3$ is decreased at all temperatures because of scattering with ionized dopant impurities. As the hole doping density is lowered toward 10^{19} cm^{-3}, effective charge-carrier mobilities exceeding 400 cm^2 V^{-1} s^{-1} are reached at low temperatures, and temperature trends suggest that the mobility is limited mostly by interactions with phonons which pose a fundamental limit. At 5 K, the photoconductivity spectra at lower hole doping density are additionally found to exhibit a localized resonance, which we attribute to the presence of bound excitons. We extract a value of 3.1 meV for the exciton binding energy in $FASnI_3$, in accordance with the relatively low bandgap of this hybrid perovskite and comparable to values obtained previously for inorganic semiconductors of similar bandgap. These findings disentangle the extrinsic and intrinsic contributions to the optoelectronic properties of $FASnI_3$ and demonstrate that many of the issues limiting the efficiency of solar cells based on tin perovskites are controllable through improvements in processing protocols.

Thin films of formamidinium tin triiodide ($FASnI_3$) were prepared via a one-step deposition method by spin coating a stoichiometric mixture of FAI and SnI_2 onto z-cut quartz substrates. To control the doping density and allow for a comparative study of $FASnI_3$ with different doping levels, three sets of samples were made for which 0, 5, or 10 mole% of SnF_2 with respect to SnI_2 were added to the mixture prior to spin coating. Full details of the sample fabrication procedure are given in the Experimental Section below. Profilometry measurements showed that the $FASnI_3$ films varied in thickness between 340–350 nm, independent of SnF_2 concentration (see Table S1, Supporting Information). Scanning electron microscopy images (Figure S1, Supporting Information) reveal that all films exhibit large grains ranging in size from 0.5–1.5 µm, which vary little in width with added SnF_2 percentage. However, some variations are apparent in surface coverage; while the films prepared with 5% and 10% SnF_2 are relatively free of pinholes, the film prepared in the absence of SnF_2 exhibits pinholes of about ≈500 nm in diameter which interspace regions of $FASnI_3$, similar to previous observations for both $FASnI_3$ and $MASnI_3$ thin films.[29,32] While such micrometer-sized variations in surface coverage have been shown to severely limit device efficiency to below 0.1% because of the resulting shorting between layers in the device,[32] they do not directly impact the shorter-range charge-carrier diffusion and recombination probed in this study. X-ray diffraction studies further demonstrate that the crystallinity does not vary significantly between thin films prepared with different concentrations of added SnF_2 (see Figure S2, Supporting Information).

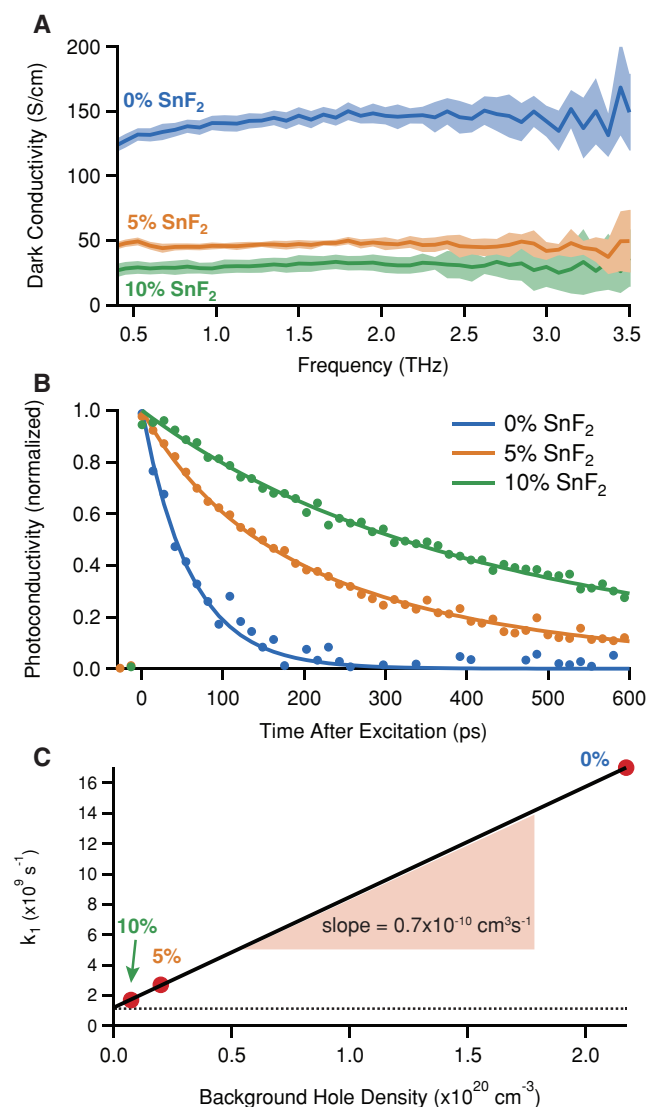In order to investigate the effect of hole doping on the optoelectronic properties of $FASnI_3$, we must first determine

Figure 1. The dependence of charge-carrier recombination on doping density in FASnI$_3$. A) Dark conductivity spectra (real part) of FASnI$_3$ thin films for which 0%, 5%, or 10% SnF$_2$ had been added to the preparation solution. Solid lines represent experimental data, and shaded regions represent the uncertainty of the measurement to one standard deviation. B) OPTPS measurements of the charge-carrier recombination dynamics of FASnI$_3$ films with different concentrations of added SnF$_2$. The thin films were photoexcited at 800 nm with a fluence of 110 μJ cm^{-2}. Solid lines are fits to Equation (1), and round markers represent the experimental data. The data have been normalized to facilitate comparisons of dynamics. C) Relationship between doping density extracted from dark conductivity spectra shown in part A, and the monomolecular charge-carrier recombination rate, k_1. The red markers are experimental data, and the solid black line is a linear fit. The dashed line indicates the y-intercept, and the shaded region marks the slope of the line.

accurately the densities obtained when different levels of SnF$_2$ are added during film fabrication. For this purpose, we performed THz time-domain spectroscopy (THz-TDS) to obtain the frequency-dependent dark conductivity of the thin films in the spectral region from 0.5–3.5 THz (**Figure 1**A). THz-TDS is a versatile noncontact method for determining the dark

conductivity of a material that has been used to probe a wide range of doped semiconductors including silicon and gallium arsenide and is particularly useful for determining electrical properties of nanomaterials and thin films where electrical contacting is difficult.[37,38] In the absence of phonon vibrations, the conductivity represents the response of mobile charges to the THz electric field and can thus be used to evaluate the dark charge-carrier concentration and hence doping density if the charge-carrier mobility is known. Figure 1A shows the real part of the frequency-dependent conductivity spectra for three FASnI$_3$ films prepared with different concentrations of SnF$_2$, as derived from the time-domain THz transmission under the applicable assumption[37] of a thin film on a thick substrate.[37] From 0.5 to 3.5 THz, the frequency-dependent conductivity spectra for all three SnF$_2$ concentrations are essentially flat, and the conductivity decreases with added SnF$_2$. Unlike lead-iodide perovskites which have strong phonon modes in this spectral region,[39,40] the phonon modes for tin perovskites are predicted to occur at higher frequencies due to the inclusion of the lighter tin atoms and are thus outside our spectral window. Therefore, the decrease in conductivity of FASnI$_3$ with added SnF$_2$ we observe here solely reflects a reduction in electrical doping density.

To explain the flat nature of the dark photoconductivity spectrum over our observation window, we consider the classical Drude model, which has been used as a starting point to describe the conductivity in many common semiconductors, including Si and GaAs.[37,38] In this model, the frequency-dependent conductivity is derived to be $\sigma(\omega) = \sigma_0(1 - i\omega\tau)^{-1}$ under the assumption that charge-carriers randomize the direction of the momentum acquired under an applied electric field through random scattering events that occur, on average, once during the momentum scattering time interval τ. The DC conductivity at zero frequency is given by $\sigma_0 = Ne^2\tau\,(m^*)^{-1} = Ne\mu$ where N is the charge-carrier density, e the elementary charge, m^* the effective mass, and μ the mobility of the charge carrier. The Drude model therefore predicts a near-constant, real conductivity for the spectral range for which angular frequencies are substantially smaller than the inverse momentum scattering time ($\omega \ll \tau^{-1}$). We find that this scenario should indeed be expected for FASnI$_3$, based on an expected effective hole mass determined both computationally[41] and experimentally[42] and on charge-carrier mobility values we report below, which yield a value of $\tau = \mu\,m^*/e \approx 2$ fs (see Figure S3 (Supporting Information) for a simulated conductivity spectrum). This behavior is in contrast to that for doped GaAs,[37,41,42] for which a relatively high hole mobility yields a momentum scattering time around 120 fs that may result in the dark conductivity rolling off within the THz spectral window (see Figure S3, Supporting Information).[38,43]

We are therefore able to extract the dark hole concentration p_0 in the FASnI$_3$ films through $p_0 = \sigma_0\,(e\mu)^{-1}$ where σ_0 is the constant value of the dark conductivity (real part) determined from THz-TDS measurements and μ is the hole mobility, which is derived from optical pump THz probe spectroscopy (OPTPS) measurements discussed below under the approximate assumption that the electron and hole mobilities are balanced.[7,41] We therefore determine hole densities of 2.2×10^{20}, 2.0×10^{19}, and 7.2×10^{18} cm^{-3} for FASnI$_3$ thin films prepared with the addition of 0%, 5%, and 10% SnF$_2$, respectively. These

**ADVANCED
SCIENCE NEWS**

www.advancedsciencenews.com

**ADVANCED
MATERIALS**

www.advmat.de

values are comparable to estimates of hole doping densities reported previously for various tin-based perovskites, which vary depending on film preparation procedure and measurement method.[14,24,25,29,33,44] Furthermore, our results show that addition of SnF_2 can be used to controllably change the doping density in $FASnI_3$ thin films over several orders of magnitude, allowing for a fundamental investigation of the relationship between doping density and optoelectronic properties.

In order to unravel the relationship between doping density and charge transport, the charge-carrier dynamics in the $FASnI_3$ films were investigated with OPTPS. In OPTPS, the change in transmission of a broadband THz probe pulse is monitored as a function of time following photoexcitation with an optical pump pulse. As the measured signal is proportional to the product of the charge-carrier density and charge-carrier mobility, OPTPS allows for the determination of charge-carrier dynamics on an ultrafast timescale. For OPTPS measurements of $FASnI_3$, the samples were excited at 800 nm with fluences ranging from 12–177 µJ cm^{-2}. Excitation fluences were chosen to fall below the threshold for spontaneous amplified emission (ASE) because ASE has been shown to shorten charge-carrier lifetimes in $FASnI_3$ thin films and interfere with the determination of charge-carrier recombination rate constants at high fluence.[25]

Figure 1B shows sample photoconductivity transients for the three $FASnI_3$ films prepared with different concentrations of SnF_2, following excitation with a fluence of 110 µJ cm^{-2} (full fluence dependences are given in Figure S4 in the Supporting Information). We find that, across all excitation fluences, the photoconductivity decay accelerates markedly with increasing dark hole density (decreasing SnF_2 addition) in accordance with a significant increase in dopant-mediated charge-carrier recombination channels.[45] In order to unravel the different contributing mechanisms, we performed global fits to the fluence-dependent transients shown in Figure S4 (Supporting Information) based on the following rate equation[9,24,25,46]

$$\frac{dn}{dt} = -k_2 n (p + p_0) - R_1 n = -k_2 n^2 - k_1 n \tag{1}$$

Here, k_2 is the bimolecular recombination constant describing radiative band-to-band recombination between electrons and holes, which may be affected by photon reabsorption effects and can be viewed as the inverse process of photon absorption.[8,47,48] Following photoexcitation, the photogenerated electron density n must balance the photogenerated hole density p. In highly p-doped materials such as $FASnI_3$, p is augmented by the substantial background hole density p_0. The total trap-mediated, monomolecular recombination is therefore characterized by a rate $k_1 = R_1 + k_2 p_0$, which has a contribution originating from radiative recombination between photogenerated electrons and background holes. Auger recombination was not included as it was found to make relatively little contribution to the recombination channels at these excitation fluences.[9,24,25,46] A full description of the fitting procedure is presented in Section S3 of the Supporting Information along with fluence dependent data in Figure S4 (Supporting Information), and a summary of the values extracted for k_1 and k_2 is presented in Table S2 (Supporting Information).

The short charge-carrier lifetimes we observe across all fluences are typical for tin-based perovskites and have been shown to affect the charge transport at solar fluences in photovoltaic devices.[24,27,33] Figure 1B highlights how this situation improves with the addition of SnF_2 and the accompanying decrease in hole doping density. For the case of 0% added SnF_2, a monomolecular rate of $k_1 = 17 \times 10^9$ s^{-1} can be extracted from the fits. This value decreases by an order of magnitude to 1.7×10^9 s^{-1} for 10% SnF_2, corresponding to a lifetime increase from 59 to 590 ps. These observations are consistent with PL measurements of $MASnI_3$ thin films, where SnF_2 treatments also resulted in an approximately tenfold increase in charge-carrier lifetime.[27,29] Such enhancement of charge-carrier lifetimes is critical to the incorporation of tin perovskites into planar-heterojunction photovoltaic devices. Using the charge-carrier mobility values extracted for these films (see below) we are able to calculate charge diffusion lengths at solar illumination levels that increase from 35 nm (0% SnF_2, $p_0 = 2.2 \times 10^{20}$ cm^{-3}) to 265 nm (10% SnF_2, $p_0 = 7.2 \times 10^{18}$ cm^{-3}) (see Table S2, Supporting Information). For the case of 10% SnF_2 addition, charge diffusion lengths approach the typical thickness of photoactive layers in perovskite solar cells ($\approx$300 nm), thus making efficient planar heterojunction devices feasible. Therefore, we conclude that hole background densities near 10^{18} cm^{-3} define the threshold of what may feasibly be tolerated in this device structure.[49]

To allow further analysis of the mechanisms underpinning monomolecular charge-carrier recombination in $FASnI_3$, Figure 1C shows the extracted values of k_1 as a function of hole doping density. The three points form a linear relationship, which is not surprising given that doping will introduce both an additional monomolecular recombination pathway that is radiative (with rate $k_2 p_0$—see Equation (1)) but may also give rise to nonradiative Shockley–Read–Hall recombination with rate constants that are proportional to the doping density.[45] A linear fit to the data in Figure 1C is indeed found to return a slope of 0.7×10^{-10} cm^3 s^{-1}, which is similar to the values obtained for k_2 from fits to fluence-dependent OPTPS transients (see Table S2, Supporting Information) and those reported previously for a range of tin-iodide perovskites.[24,25,27,28] Interestingly, k_1 does not approach zero as the dopant density tends to zero but rather intercepts the y-axis at a value of $k_1 = 1.2 \times 10^9$ s^{-1}, equivalent to a maximum lifetime of the order of one nanosecond for $p_0 = 0$. This observation suggests the existence of an additional trap-mediated charge recombination mechanism that is not remedied by SnF_2 passivation. Since excess tin is thought to decrease p-doping through the reduction of tin vacancies,[14] such additional trap states may originate from different types of defects. Theoretical calculations investigating vacancies, substitutions, and interstitials in $CsSnI_3$ have suggested that when conditions change from tin-poor to tin-rich, the formation energy for tin vacancies is raised, while that of Sn_I antisites and iodine vacancies is lowered.[50] Therefore, we postulate that future improvements of charge-carrier lifetimes in tin perovskites may require additional passivation strategies that go beyond the usual focus of tin vacancy elimination through SnF_2 addition.[25,27–30]

The presence of a large background density of holes may modify the absorption spectrum and the energy levels of mobile electrons and holes, which will have a substantial impact on the
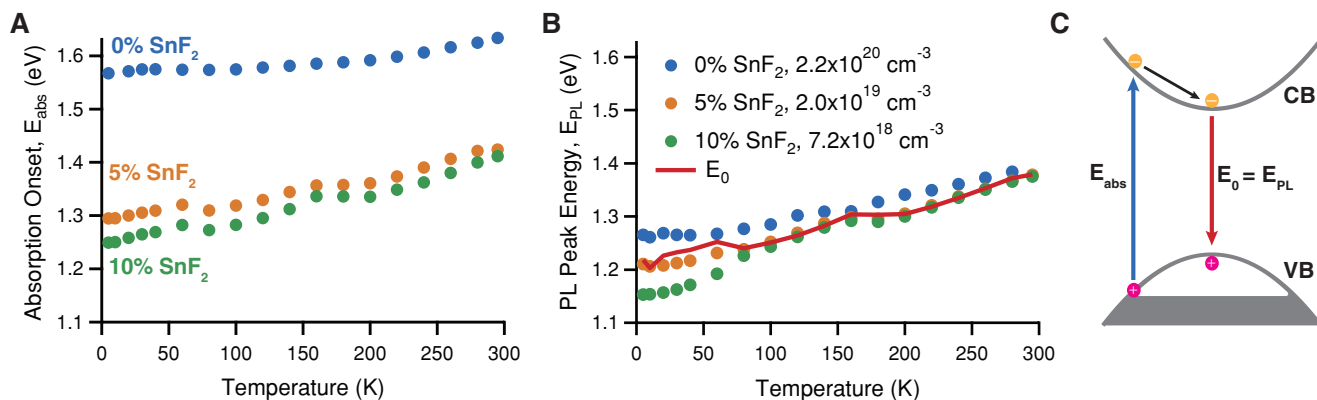
Figure 2. Temperature-dependent Burstein–Moss effect in FASnI$_3$. A) The midpoint energy of the absorption edge. B) The energy of PL maximum of FASnI$_3$ thin films for which 0%, 5%, or 10% SnF$_2$ had been added to the preparation solution, resulting in hole doping densities of 7.2×10^{18}, 2.0×10^{19}, and 2.2×10^{20} cm^{-3}, respectively. The samples were photoexcited at 800 nm with fluences ranging from 7–10 μJ cm^{-2}. The red line indicates the true bandgap energy E_0, extracted by fitting data points in part A with the expression $E_{abs} - E_0 = Kp_0^{2/3}$, which also yielded a weakly temperature sensitive value of $K = (8 \pm 1) \times 10^{-15}$ eV cm^2. C) Schematic indicating charge-carrier absorption and emission processes between the conduction (CB) and valance (VB) bands of a highly doped semiconductor.

requirements for photovoltaic device design. To investigate such effects, we probe the changes in absorption and photoluminescence spectra with temperature for the three different doping concentrations. **Figure 2**A displays the temperature-dependent energy E_{abs} of the onset of absorption, which is taken from the midpoint of the band edge (Figure S5, Supporting Information) in order to avoid complications from thermal broadening[47] and band-tailing associated with doping.[51]

The general trends of the absorption onset with temperature are similar to those observed previously for a range of lead, tin, and mixed lead-tin perovskites.[26,45,49] The absorption edge of all three films exhibits a blueshift with increasing temperature, which is opposite to the Varshni trend typically observed in many inorganic semiconductors.[52] These trends are generally influenced by two competing contributions—one originating from the dilation of the lattice and its effect on energy levels and the other from electron-phonon interactions—both of which may depend on temperature with varying sign and extent.[26,45,49,52,53] In addition, phase transitions are observed in FASnI$_3$ as changes in the gradients of these data at approximate temperatures of 70 and 160 K, similar to previous reports[45,54–56] for single and poly-crystalline FASnI$_3$.[45,54–56] We note that these transitions are less clearly observable for the highly doped (0% SnF$_2$) material, most likely because the presence of ionized tin vacancies leads to energetic broadening arising from local strain and electric fields.[51,54,55] Such broadening may also be the reason why we cannot discern the additional phase transition (to cubic) that has been reported to occur near 225–250 K.[55,56]

In addition to these temperature trends, the FASnI$_3$ films show a pronounced blueshift in absorption onset with increasing background hole concentration (Figure 2A). For the film without SnF$_2$ addition ($p_0 = 2.2 \times 10^{20}$ cm^{-3}), the band edge is shifted upward by up to 300 meV with respect to that for the FASnI$_3$ films prepared with 10% SnF$_2$. We attribute this phenomenon to the Burstein–Moss effect,[29,51,57–59] which is illustrated in Figure 2C. Here, significant hole doping leads to a downshift of the Fermi-level and a significant depletion of the

electronic states near the top of the valence band. As a result, electronic transitions between the highest occupied states in the valence band and the conduction band now occur at energies E_{abs} exceeding the bandgap energy E_0. Such effects are well known for classical inorganic semiconductors such as InSb and GaAs, where they lead to sizeable increases in the energy of absorption onsets at high doping levels.[51,58,59] If we assume the presence of parabolic bands, the Burstein–Moss effect should lead to an upshift in energy of $E_{abs} - E_0 = Kp_0^{2/3}$,[59] (where K is a constant) hence we are able to extract the limit of the bandgap energy E_0 in the absence of doping from linear interpolation of the measured E_{abs} as a function of $p_0^{2/3}$.

Figure 2B shows the resulting value of the bandgap energy E_0 as a function of temperature (red line) together with the PL peak energies determined from the photoluminescence spectra. There is excellent correspondence between these values, which can be understood from the schematic given in Figure 2C: because photoexcited electrons will relax to the conduction band edge and subsequently recombine with holes near the valence band edge, the PL peak will be close in energy to the bandgap and relatively independent of doping density, as observed. We note that at very low temperature, however, slight differences in PL peak energy become evident. These may be the result of defect levels inside the bandgap, local strains, or electrostatic potential variations associated with the tin vacancies,[29,51,57,58,60,61] giving rise to band-tail recombination that becomes more evident at low temperature (see Figure S7, Supporting Information).[42,62]

Unlike the Burstein–Moss shifts encountered in hybrid perovskites following intense photoexcitation,[42,63] those induced by the high background hole density are nontransient. As a result of the associated intraband relaxation of carriers (Figure 2C) these permanent blueshift of the absorption will cause sizeable Stokes shifts for heavily doped FASnI$_3$ films (0% SnF$_2$). At room temperature, FASnI$_3$ (0% SnF$_2$) exhibits a Stokes shift near 250 meV, which is reduced considerably to ≈60 meV with the addition of 5% SnF$_2$, and ≈40 meV for 10% SnF$_2$[49,61] (Figure S6, Supporting Information), which is approaching the values of

**ADVANCED
SCIENCE NEWS**
www.advancedsciencenews.com

**ADVANCED
MATERIALS**
www.advmat.de

4–10 meV reported for relatively defect free MAPbI$_3$.[49] The full-width half-maximum (FWHM) of the PL also increases with increased doping density at all temperatures investigated, indicating increased electronic disorder caused by the presence of defect states (Figure S6, Supporting Information). For photovoltaic devices, such doping-induced effects are highly detrimental because the upshift of the absorption onset followed by charge-carrier relaxation to the true band edge E_0, will introduce additional open-circuit voltage losses. Our measurements suggest that addition of at least 5% SnF$_2$ ($p_0 = 2.0 \times 10^{19}$ cm^{-3}) should reduce such losses to the tens of millielectron volts.

To explore how such unintentional hole doping affects charge transport, we determined the effective charge-carrier mobilities for all three thin films as a function of temperature using OPTPS (see Section S6 in the Supporting Information for details on data processing). Here, the peak initial $\Delta T/T$ value measured with OPTPS after pulsed excitation was used to infer the effective charge-carrier mobility $\phi\mu$, where ϕ is the photon-to-charge branching ratio and μ is the sum over the charge-carrier mobilities of electrons and holes. As extracted values varied slightly between samples prepared with 0% and 10% added SnF$_2$, at least two films were measured for those compositions and average values were taken (Table S2, Supporting Information).

To begin our analysis of the charge-carrier mobility, we compare the values obtained at room temperature for FASnI$_3$ films with different doping densities. We find that as the doping density is reduced from $p_0 = 2.2 \times 10^{20}$ cm^{-3} (0% SnF$_2$), the average charge-carrier mobility increases from 23 to 37 cm^2 V^{-1} s^{-1} for $p_0 = 2.0 \times 10^{19}$ cm^{-3} (5% SnF$_2$) and further to 67 cm^2 V^{-1} s^{-1} for $p_0 = 7.2 \times 10^{18}$ cm^{-3} (10% SnF$_2$). These values all fall within the wide range reported for tin perovskite crystals, films, and powders[7,22,24,33,64] suggesting that differences in doping density may be the cause of some of the large variation in these values encountered in the literature. The charge-carrier mobility of other hybrid perovskites has been shown to depend on factors such as doping density, morphology, and crystallinity,[64–66] all of which can be altered by SnF$_2$ addition to tin perovskites.[19,29,32,36] As OPTPS measurements probe only short-range photoconductivity, they are less sensitive to morphological changes. In addition, comparison of the X-ray diffraction (XRD) spectra for all films (Figure S2, Supporting Information) reveals that addition of SnF$_2$ does not substantially alter the peak positions, intensities, or FWHMs, indicating that the local crystallinity is similar for all of the materials. Therefore, we suggest that these increases in charge mobility with decreasing background hole density are mostly the result of decreased scattering with ionized acceptor sites. Such reductions in charge-carrier mobility with electrical doping are well known to occur in classical inorganic semiconductors such as GaAs,[67] which has led to the introduction of modulation doping, for which ionized donor or acceptor sites are spatially separated from the mobile electrons and holes they introduce.[68–71]

To further probe the mechanisms determining the charge-carrier mobility in FASnI$_3$ films, we measured the temperature dependence of the charge-carrier mobility from 5–295 K (**Figure 3**A). For all doping levels, the mobility increases distinctly with decreasing temperature until below 50 K, where it either remains constant or slightly decreases toward 5 K.
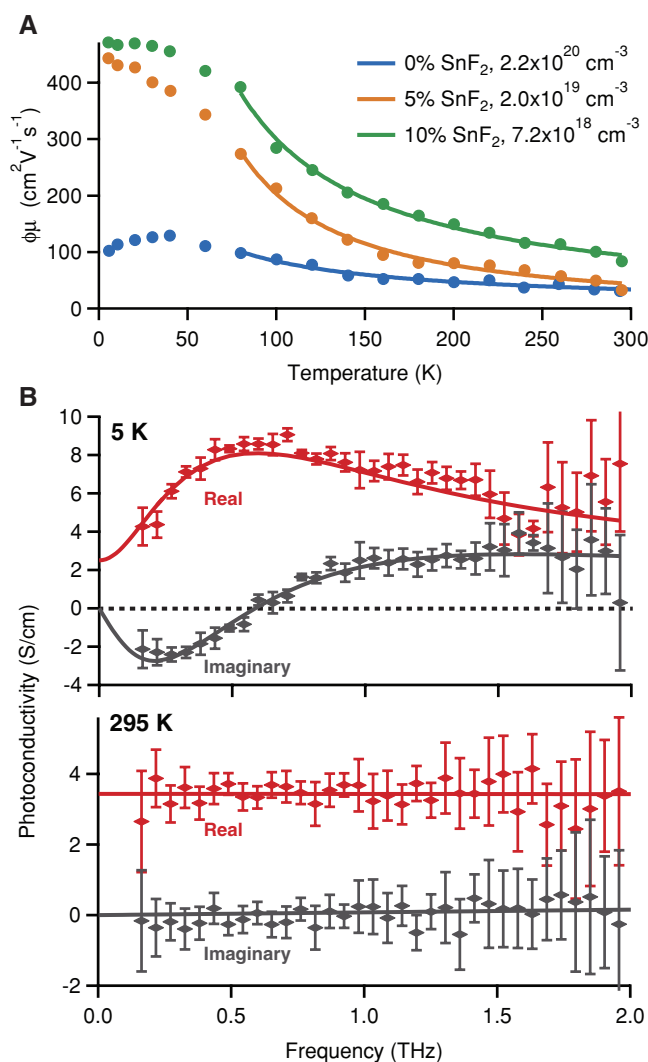

Figure 3. A) Effective charge-carrier mobility of FASnI$_3$ thin films as a function of temperature obtained from optical-pump THz-probe photoconductivity measurements using photoexcitation at 800 nm at low fluences ranging from 7 to 10 μJ cm^{-2}. Solid lines are fits to a T^m dependence as described in the main text, yielding values of $m = -0.8$, -1.4 and -1.1 for FASnI$_3$ films fabricated with addition of 0%, 5%, and 10% of SnF$_2$. B) Frequency-dependent photoconductivity spectra for a FASnI$_3$ (10% SnF$_2$) thin film, measured at 5 K (top) and 295 K (bottom). The sample was photoexcited at 800 nm in the linear fluence regime, and the reported spectra represent an average of traces obtained at 26 and 680 ps as there were no significant changes in either spectral shape or magnitude of photoconductivity over this temporal range (see Figure S10, Supporting Information). At 5 K, the experimental data (solid diamonds with error bars indicating one standard deviation) are shown with fits (lines) based on a resonance resulting from interexcitonic transitions plus a Drude component as described in the Supporting Information. For the 295 K data, the solid lines indicate the expected Drude conductivity spectrum calculated using the mobility value determined from OPTPS measurements.

Such behavior is similar to that for high-quality methylammonium lead iodide perovskite,[49,72–74] for which the charge-carrier mobility has been found to increase with decreasing temperature according to $T^{-1.5}$, as interactions between charge-carriers and longitudinal optical (LO) phonons are reduced.[75] To determine the corresponding functional dependence for

$FASnI_3$ as a function of temperature T, we fitted the carrier mobility data with a T^m expression (solid lines in Figure 3A) and find values of $m = -0.8$, -1.4, and -1.1 for $FASnI_3$ films fabricated with addition of 0%, 5%, and 10% of SnF_2. These exponents are relatively similar within the fitting error (± 0.2), although the heavily doped material exhibits the shallowest rise with decreasing T, in accordance with increased carrier interactions with ionized impurities at low temperature that results from the lower thermal velocity of charge-carriers.[76–78] Such interactions with dopants hence suppress the charge-carrier mobility at low temperatures, therefore the heavily doped $FASnI_3$ film ($p_0 = 2.2 \times 10^{20}$ cm^{-3}, 0% SnF_2) only reaches a maximum value of 130 cm^2 V^{-1} s^{-1} at 40 K, which decreases slightly toward even lower temperatures. The lowest hole-density $FASnI_3$ film ($p_0 = 7.2 \times 10^{18}$ cm^{-3}, 10% SnF_2), on the other hand, reaches an impressive charge-carrier mobility maximum of 470 cm^2 V^{-1} s^{-1} at 5K, which exceeds values reported for lead halide perovskite thin films at any temperature.[7] We attribute this improvement in charge-carrier mobility with respect to lead-halide perovskites to the higher frequency expected for the LO vibration associated with the iodine and (lighter) tin atoms, which will shift the onset of Fröhlich interactions between charge-carriers and LO phonons to higher temperatures compared to lead-based perovskites.[7]

Finally, we examine the value of the exciton binding energy for this low-bandgap hybrid perovskite. While excitons are expected to be dissociated at thermal energies exceeding the exciton binding energy, sufficiently low temperatures may allow for these excitations to be stabilized. While a range of exciton binding energies centering around 10–15 meV have been reported for lead iodide perovskites,[46,47,79] direct measurements of the exciton binding energy in $FASnI_3$ are still elusive.[7,49,76–78,80,81]

The plateauing of the effective charge-carrier $\phi\mu$ for the passivated $FASnI_3$ film ($p_0 = 7.2 \times 10^{18}$ cm^{-3}, 10% SnF_2) below 50 K may suggest an increasing influence of excitonic effects, through a decrease in photon-to-charge branching ratio ϕ. To distinguish such effects from a simple reduction resulting in charge-carrier mobility caused by enhanced scattering with doped impurities, we evaluated the frequency-dependent photoconductivity for this sample at temperatures from 5 to 295 K (Figure 3 and Figure S9, Supporting Information). At room temperature, the flat real part and zero-valued imaginary part are indicative of Drude-like charge transport with a short scattering time, which is consistent with the dark conductivity TDS measurements described above and with other OPTPS measurements of both tin and lead perovskites (see the Supporting Information and previous discussion), suggesting a predominant contribution from photoexcited free carriers.[24,49,74,82] However, at the lowest temperatures the spectra begin to deviate from this Drude behavior and show the characteristic spectra of a Lorentzian oscillator resonance, which is characterized by increased curvature in the real part of the photoconductivity and a zero crossing in the imaginary component (Figure 3B). The Lorentzian shape indicates localization of charge-carriers, which could in general result from many different species, including excitons, plasmons, or impurity-bound carriers.[37,38] However, we find that this particular resonance is most likely caused by bound excitons for the following reasons.

First, the contribution from this feature decreases rapidly when thermal energies approach the value of the resonance energy we extract (Figure S9, Supporting Information). In addition, the zero crossing of the imaginary part of the spectrum does not shift when the charge-carrier density declines with time after excitation (see Figure S10, Supporting Information), ruling out the possibility of a plasma resonance. Third, we find that for the heavily p-doped $FASnI_3$ film ($p_0 = 2.2 \times 10^{20}$ cm^{-3}, 0% SnF_2), the Lorentzian resonance gives way to a Drude-like spectrum even at low temperatures (Figure S11, Supporting Information), suggesting effective exciton dissociation above the Mott density.[47,83]

According to this analysis, we fitted a model to account for interexcitonic transitions between bound and continuum states[40] plus a constant Drude term to include the response of remaining free charge carriers to the photoconductivity spectra for the lowest density $FASnI_3$ film ($p_0 = 7.2 \times 10^{18}$ cm^{-3}, 10% SnF_2) at 5 K (full details are provided in Section S7 of the Supporting Information). Using this model, we extract an exciton binding energy of 3.1 meV for $FASnI_3$, which is significantly lower than values typically reported for lead iodide perovskites.[46] Such a reduction may be expected, given the empirical correlation between bandgaps and exciton binding energies that stems from general trends of the effective masses and dielectric properties with bandgaps of semiconductors.[84] Hence, the slight lowering of the bandgap of undoped $FASnI_3$ by about 150 meV with respect to that $FAPbI_3$ alone is expected to lead to a reduction in exciton binding energy.[46,85,86] We further note that InP and GaAs exhibit similar exciton binding energies (5.1 and 4.2 meV, respectively) for low-temperature bandgaps (1.4 and 1.5 eV, respectively)[87,88] comparable to the values we determine for here, showing that these hybrid semiconductors exhibit analogous optoelectronic properties to those of comparable inorganic semiconductors. The lower exciton binding energy for $FASnI_3$ with respect to that of $FAPbI_3$ further means that free-charge conductivity persists to lower temperatures, making $FASnI_3$ a more flexible material for photovoltaic cells operating at a variety of temperatures and setting, as for example outer space.

In conclusion, we have unraveled the intrinsic and extrinsic optoelectronic properties of $FASnI_3$ thin films fabricated with a range of quantified background hole doping densities. We show that monomolecular charge recombination has both a dopant-mediated part that grows linearly with doping density but also remnant contributions that will require alternative treatments to mitigate the effects of fast recombination. We show that hole doping leads to a clear Burstein–Moss effect that increases absorption onsets by ≈300 meV for hole densities near 10^{20} cm^{-3} and masks the true bandgap energy of the tin perovskite, which we reveal to range between 1.2 eV at 5 K and 1.35 eV at room temperature. Temperature-dependent measurements of the effective charge-carrier mobility suggest that at high dopant densities, the mobility is lowered through scattering with ionized dopant impurities. However, once the background hole concentration is suppressed to near 10^{19} cm^{-3} or below, the charge-carrier mobility increases more steeply with temperature according to ≈T^m, with $m = -1.1$ to -1.4, suggesting that intrinsic interactions with lattice vibrations dominate. From intraexcitonic transitions observed in the

**ADVANCED
SCIENCE NEWS**

www.advancedsciencenews.com

**ADVANCED
MATERIALS**

www.advmat.de

THz frequency transmission spectra at 5 K, we determine an exciton binding energy of only 3.1 meV for $FASnI_3$, which is lower than values typically observed for higher-bandgap lead iodide perovskites and compares well with values for traditional inorganic semiconductors of comparable bandgap energy. With further control over extrinsic materials properties, tin perovskites therefore have the potential to equal or surpass the performance of lead perovskites in many optoelectronic applications.

Experimental Section

Film Preparation: Formamidinium iodide (FAI) was purchased from Greatcell Solar. Tin (II) iodide (SnI_2, 99.999% Ultradry) was purchased from Alfa Aesar. Tin (II) fluoride (SnF_2, 99%), *n,n*-dimethylformamide (DMF, anhydrous, ≥99.8%), dimethyl sulfoxide (DMSO, anhydrous, ≥99.9%), and diethyl ether (anhydrous, ≥99.7%) were purchased from Sigma-Aldrich.

A solution of $FASnI_3$ (1.0 M) was prepared in a nitrogen atmosphere by dissolving stoichiometric amounts of FAI and SnI_2 in a mixed solvent of 4:1 DMF:DMSO by volume. An additional amount of SnF_2 (0%, 5%, 10% molar amount with respect to SnI_2) was dissolved in the solution. The solution was stirred overnight at room temperature and filtered with a PTFE filter (0.45 µm) prior to use. The samples were prepared in a nitrogen atmosphere by statically dispensing the solution on an O_2-plasma treated z-cut quartz disc and spin-coating at 4 krpm for 30 s with a 6 s ramp. At 12 s from the start of the spin-coating program, 200 µL of diethyl ether was dropped onto the spinning film, which caused the perovskite film to immediately darken. The films were subsequently annealed at 70 °C for 20 min in an N_2 atmosphere.

Film Characterization: Film thicknesses were measured using a Veeco Dektak 150 surface profilometer. Several positions on each film were sampled in order to determine an average value across the film. Scanning electron microscopy images were obtained with a Hitachi S-4300 scanning electron microscope operating with a 10 kV acceleration voltage and a probe current of 11 µA. XRD spectra of the prepared films were measured using a Rigaku SmartLab X-ray diffractometer with $CuK_{\alpha 1}$ (1.54060 Å) and a HyPix-3000 2D hybrid pixel array detector. For SEM and XRD measurements, thin films of $FASnI_3$ with various amounts of SnF_2 were prepared on O_2-plasma treated TEC15 fluorine-doped tin oxide substrates using the same method as described previously.

THz Spectroscopy: The THz spectroscopy system was based on an amplified laser system (Mai Tai–Empower–Spitfire from Spectra Physics) with an 800 nm center wavelength, a 35 fs pulse duration, and a 5 kHz repetition rate. THz radiation was generated in a metallic spintronic emitter using the inverse spin hall effect[89,90] and detected via free-space electro-optic sampling with a 0.2 mm thick GaP(110) crystal and a pair of balanced photodiodes. The same system was used for both THz-TDS and OPTPS measurements, and all measurements were performed in vacuum. For OPTPS measurements, the samples were photoexcited at 800 nm at fluences ranging from 12 to 177 µJ cm^{-2} using the same amplified laser system. The samples were mounted on a cold-finger cryostat (Oxford Instruments, MicrostatHe) for low temperature measurements. The temperature was lowered using liquid helium and the desired temperature set using a temperature controller (Oxford Instruments, ITC503) connected to resistive heater and temperature sensors mounted both on the cryostat heat exchanger and at the end of the sample holder.

Photoluminescence: PL measurements were performed in situ with OPTPS measurements using the same 800 nm excitation source from the amplified laser system. Scattered PL from the sample was collected via a collimating lens fixed ≈127 mm from the sample. An optical fiber was then used to direct the light toward an imaging spectrometer (Horiba, iHR320), and the light was detected using either a nitrogen-cooled silicon CCD or InGaAs array as appropriate.

Steady-State Absorption: The optical absorbance spectra were taken using a Bruker Vertex 80v Fourier-transform infrared spectrometer fitted with a transmission/reflection accessory. The source was a tungsten halogen lamp, and a silicon diode detector was used. The samples were mounted in a gas exchange cryostat (Oxford Instruments, OptistatCF2), cooled with liquid helium, and heated with a resistive heater via a temperature controller (Oxford Instruments, MercuryiTC).

[1] I. Mesquita, L. Andrade, A. Mendes, *Renewable Sustainable Energy Rev.* **2018**, *82*, 2471.

[2] B. R. Sutherland, E. H. Sargent, *Nat. Photonics* **2016**, *10*, 295.

[3] S. A. Veldhuis, P. P. Boix, N. Yantara, M. Li, T. C. Sum, N. Mathews, S. G. Mhaisalkar, *Adv. Mater.* **2016**, *28*, 6804.

[4] National Renewable Energy Laboratory (NREL), Best Research-Cell Efficiencies, http://www.nrel.gov/pv (accessed: July 2018).

[5] H. Wang, D. H. Kim, *Chem. Soc. Rev.* **2017**, *46*, 5204.

[6] Q. Q. Lin, Z. P. Wang, M. Young, J. B. Patel, R. L. Milot, L. M. Maestro, R. R. Lunt, H. J. Snaith, M. B. Johnston, L. M. Herz, *Adv. Funct. Mater.* **2017**, *27*, 1702485.

[7] L. M. Herz, *ACS Energy Lett.* **2017**, *2*, 1539.

[8] M. B. Johnston, L. M. Herz, *Acc. Chem. Res.* **2016**, *49*, 146.

[9] J. S. Manser, J. A. Christians, P. V. Kamat, *Chem. Rev.* **2016**, *116*, 12956.

[10] A. Babayigit, A. Ethirajan, M. Muller, B. Conings, *Nat. Mater.* **2016**, *15*, 247.

[11] A. Babayigit, H. G. Boyen, B. Conings, *MRS Energy Sustainability* **2018**, *5*, E1.

[12] J. Werner, B. Niesen, C. Ballif, *Adv. Mater. Interfaces* **2018**, *5*, 201700731.

[13] F. Giustino, H. J. Snaith, *ACS Energy Lett.* **2016**, *1*, 1233.

[14] M. Konstantakou, T. Stergiopoulos, *J. Mater. Chem. A* **2017**, *5*, 11518.

[15] S. Chatterjee, A. J. Pal, *J. Mater. Chem. A* **2018**, *6*, 3793.

[16] S. Korbel, M. A. L. Marques, S. Botti, *J. Mater. Chem. C* **2016**, *4*, 3157.

[17] M. R. Filip, F. Giustino, *J. Phys. Chem. C* **2016**, *120*, 166.

[18] M. R. Filip, G. E. Eperon, H. J. Snaith, F. Giustino, *Nat. Commun.* **2014**, *5*, 5757.

[19] S. Y. Shao, J. Liu, G. Portale, H. H. Fang, G. R. Blake, G. H. ten Brink, L. J. A. Koster, M. A. Loi, *Adv. Energy Mater.* **2018**, *8*, 1702019.

[20] G. E. Eperon, T. Leijtens, K. A. Bush, T. Green, J. T. W. Wang, D. P. McMeekin, G. Volonakis, R. L. Milot, D. J. Slotcavage, R. Belisle, J. B. Patel, E. S. Parrott, R. J. Sutton, W. Ma, F. Moghadam, B. Conings, A. Babayigit, H. G. Boyen, F. Giustino, L. M. Herz, M. B. Johnston, M. D. McGehee, H. J. Snaith, *Science* **2016**, *345*, 861.

[21] L. S. Liang, P. Gao, *Adv. Sci.* **2018**, *5*, 1700331.

[22] Y. Takahashi, H. Hasegawa, Y. Takahashi, T. Inabe, *J. Solid State Chem.* **2013**, *205*, 39.

[23] T. Leijtens, R. Prasanna, A. Gold-Parker, M. F. Toney, M. D. McGehee, *ACS Energy Lett.* **2017**, *2*, 2159.

[24] N. K. Noel, S. D. Stranks, A. Abate, C. Wehrenfennig, S. Guarnera, A. A. Haghighirad, A. Sadhanala, G. E. Eperon, S. K. Pathak, M. B. Johnston, A. Petrozza, L. M. Herz, H. J. Snaith, *Energy Environ. Sci.* **2014**, *7*, 3061.

[25] R. L. Milot, G. E. Eperon, T. Green, H. J. Snaith, M. B. Johnston, L. M. Herz, *J. Phys. Chem. Lett.* **2016**, *7*, 4178.

[26] E. S. Parrott, R. L. Milot, T. Stergiopoulos, H. J. Snaith, M. B. Johnston, L. M. Herz, *J. Phys. Chem. Lett.* **2016**, *7*, 1321.

[27] L. Ma, F. Hao, C. C. Stoumpos, B. T. Phelan, M. R. Wasielewski, M. G. Kanatzidis, *J. Am. Chem. Soc.* **2016**, *138*, 14750.

[28] T. B. Song, T. Yokoyama, C. C. Stoumpos, J. Logsdon, D. H. Cao, M. R. Wasielewski, S. Aramaki, M. G. Kanatzidis, *J. Am. Chem. Soc.* **2017**, *139*, 836.

[29] T. Handa, T. Yamada, H. Kubota, S. Ise, Y. Miyamoto, Y. Kanemitsu, *J. Phys. Chem. C* **2017**, *121*, 16158.

[30] B. Wu, Y. Y. Zhou, G. C. Xing, Q. Xu, H. F. Garces, A. Solanki, T. W. Goh, N. P. Padture, T. C. Sum, *Adv. Funct. Mater.* **2017**, *27*, 1604818.

[31] A. G. Kontos, A. Kaltzoglou, E. Siranidi, D. Palles, G. K. Angeli, M. K. Arfanis, V. Psycharis, Y. S. Raptis, E. I. Kamitsos, P. N. Trikalitis, C. C. Stoumpos, M. G. Kanatzidis, P. Falaras, *Inorg. Chem.* **2017**, *56*, 84.

[32] T. M. Koh, T. Krishnamoorthy, N. Yantara, C. Shi, W. L. Leong, P. P. Boix, A. C. Grimsdale, S. G. Mhaisalkar, N. Mathews, *J. Mater. Chem. A* **2015**, *3*, 14996.

[33] M. H. Kumar, S. Dharani, W. L. Leong, P. P. Boix, R. R. Prabhakar, T. Baikie, C. Shi, H. Ding, R. Ramesh, M. Asta, M. Graetzel, S. G. Mhaisalkar, N. Mathews, *Adv. Mater.* **2014**, *26*, 7122.

[34] S. J. Lee, S. S. Shin, Y. C. Kim, D. Kim, T. K. Ahn, J. H. Noh, J. Seo, S. I. Seok, *J. Am. Chem. Soc.* **2016**, *138*, 3974.

[35] S. Gupta, D. Cahen, G. Hodes, *J. Phys. Chem. C* **2018**, *122*, 13926.

[36] S. Gupta, T. Bendikov, G. Hodes, D. Cahen, *ACS Energy Lett.* **2016**, *1*, 1028.

[37] H. J. Joyce, J. L. Boland, C. L. Davies, S. A. Baig, M. B. Johnston, *Semicond. Sci. Technol.* **2016**, *31*, 103003.

[38] J. Lloyd-Hughes, T. I. Jeon, *J. Infrared, Millimeter, Terahertz Waves* **2012**, *33*, 871.

[39] M. A. Perez-Osorio, R. L. Milot, M. R. Filip, J. B. Patel, L. M. Herz, M. B. Johnston, F. Giustino, *J. Phys. Chem. C* **2015**, *119*, 25703.

[40] R. A. Kaindl, D. Hagele, M. A. Carnahan, D. S. Chemla, *Phys. Rev. B* **2009**, *79*, 045320.

[41] P. Umari, E. Mosconi, F. De Angelis, *Sci. Rep.* **2014**, *4*, 4467.

[42] H. H. Fang, S. Adjokatse, S. Y. Shao, J. Even, M. A. Loi, *Nat. Commun.* **2018**, *9*, 243.

[43] M. C. Beard, G. M. Turner, C. A. Schmuttenmaer, *Phys. Rev. B* **2000**, *62*, 15764.

[44] W. Q. Liao, D. W. Zhao, Y. Yu, C. R. Grice, C. L. Wang, A. J. Cimaroli, P. Schulz, W. W. Meng, K. Zhu, R. G. Xiong, Y. F. Yan, *Adv. Mater.* **2016**, *28*, 9333.

[45] E. S. Parrott, T. Green, R. L. Milot, M. B. Johnston, H. J. Snaith, L. M. Herz, *Adv. Funct. Mater.* **2018**, *28*, 1802803.

[46] L. M. Herz, *Ann. Rev. Phys. Chem.* **2016**, *67*, 65.

[47] C. L. Davies, M. R. Filip, J. B. Patel, T. W. Crothers, C. Verdi, A. D. Wright, R. L. Milot, F. Giustino, M. B. Johnston, L. M. Herz, *Nat. Commun.* **2018**, *9*, 293.

[48] T. W. Crothers, R. L. Milot, J. B. Patel, E. S. Parrott, J. Schlipf, P. Muller-Buschbaum, M. B. Johnston, L. M. Herz, *Nano Lett.* **2017**, *17*, 5782.

[49] R. L. Milot, G. E. Eperon, H. J. Snaith, M. B. Johnston, L. M. Herz, *Adv. Funct. Mater.* **2015**, *25*, 6218.

[50] P. Xu, S. Y. Chen, H. J. Xiang, X. G. Gong, S. H. Wei, *Chem. Mater.* **2014**, *26*, 6068.

[51] J. I. Pankove, *Phys. Rev.* **1965**, *140*, 2059.

[52] Y. P. Varshni, *Physica* **1967**, *34*, 149.

[53] C. L. Yu, Z. Chen, J. J. Wang, W. Pfenninger, N. Vockic, J. T. Kenney, K. Shum, *J. Appl. Phys.* **2011**, *110*, 063526.

[54] D. B. Mitzi, K. Liang, *J. Solid State Chem.* **1997**, *134*, 376.

[55] C. C. Stoumpos, C. D. Malliakas, M. G. Kanatzidis, *Inorg. Chem.* **2013**, *52*, 9019.

[56] E. C. Schueller, G. Laurita, D. H. Fabini, C. C. Stoumpos, M. G. Kanatzidis, R. Seshadri, *Inorg. Chem.* **2018**, *57*, 695.

[57] H. Teisseyre, P. Perlin, T. Suski, I. Grzegory, S. Porowski, J. Jun, A. Pietraszko, T. D. Moustakas, *J. Appl. Phys.* **1994**, *76*, 2429.

[58] E. Burstein, *Phys. Rev.* **1954**, *93*, 632.

[59] T. S. Moss, *Proc. Phys. Soc., London, Sect. B* **1954**, *67*, 775.

[60] Z. H. Lu, M. C. Hanna, A. Majerfeld, *Appl. Phys. Lett.* **1994**, *64*, 88.

[61] Y. H. Yang, X. Y. Chen, Y. Feng, G. W. Yang, *Nano Lett.* **2007**, *7*, 3879.

[62] A. D. Wright, R. L. Milot, G. E. Eperon, H. J. Snaith, M. B. Johnston, L. M. Herz, *Adv. Funct. Mater.* **2017**, *27*, 1700860.

[63] J. S. Manser, P. V. Kamat, *Nat. Photonics* **2014**, *8*, 737.

[64] X. F. Qiu, B. Q. Cao, S. Yuan, X. F. Chen, Z. W. Qiu, Y. A. Jiang, Q. Ye, H. Q. Wang, H. B. Zeng, J. Liu, M. G. Kanatzidis, *Sol. Energ. Mater. Sol. Cells* **2017**, *159*, 227.

[65] R. L. Milot, R. J. Sutton, G. E. Eperon, A. A. Haghighirad, J. Martinez Hardigree, L. Miranda, H. J. Snaith, M. B. Johnston, L. M. Herz, *Nano Lett.* **2016**, *16*, 7001.

[66] W. Rehman, D. P. McMeekin, J. B. Patel, R. L. Milot, M. B. Johnston, H. J. Snaith, L. M. Herz, *Energy Environ. Sci.* **2017**, *10*, 361.

[67] H. C. Casey, F. Stern, *J. Appl. Phys.* **1976**, *47*, 631.

[68] J. L. Boland, S. Conesa-Boj, P. Parkinson, G. Tutuncuoglu, F. Matteini, D. Ruffer, A. Casadei, F. Amaduzzi, F. Jabeen, C. L. Davies, H. J. Joyce, L. M. Herz, A. F. I. Morral, M. B. Johnston, *Nano Lett.* **2015**, *15*, 1336.

[69] J. L. Boland, G. Tutuncuoglu, J. Q. Gong, S. Conesa-Boj, C. L. Davies, L. M. Herz, A. F. I. Morral, M. B. Johnston, *Nanoscale* **2017**, *9*, 7839.

[70] L. Pfeiffer, K. W. West, H. L. Stormer, K. W. Baldwin, *Appl. Phys. Lett.* **1989**, *55*, 1888.

[71] W. I. Wang, E. E. Mendez, F. Stern, *Appl. Phys. Lett.* **1984**, *45*, 639.

[72] H. Oga, A. Saeki, Y. Ogomi, S. Hayase, S. Seki, *J. Am. Chem. Soc.* **2014**, *136*, 16948.

[73] T. J. Savenije, C. S. Ponseca, L. Kunneman, M. Abdellah, K. B. Zheng, Y. X. Tian, Q. S. Zhu, S. E. Canton, I. G. Scheblykin, T. Pullerits, A. Yartsev, V. Sundstrom, *J. Phys. Chem. Lett.* **2014**, *5*, 2189.

[74] M. Karakus, S. A. Jensen, F. D'Angelo, D. Turchinovich, M. Bonn, E. Canovas, *J. Phys. Chem. Lett.* **2015**, *6*, 4991.

[75] A. D. Wright, C. Verdi, R. L. Milot, G. E. Eperon, M. A. Perez-Osorio, H. J. Snaith, F. Giustino, M. B. Johnston, L. M. Herz, *Nat. Commun.* **2016**, *7*, 11755.

[76] H. Brooks, *Phys. Rev.* **1951**, *83*, 879.

[77] E. Conwell, V. F. Weisskopf, *Phys. Rev.* **1950**, *77*, 388.

[78] S. S. Li, W. R. Thurber, *Solid State Electron.* **1977**, *20*, 609.

[79] K. Galkowski, A. Mitioglu, A. Miyata, P. Plochocka, O. Portugall, G. E. Eperon, J. T. W. Wang, T. Stergiopoulos, S. D. Stranks, H. J. Snaith, R. J. Nicholas, *Energy Environ. Sci.* **2016**, *9*, 962.

[80] D. K. Ferry, *Phys. Rev. B* **1976**, *14*, 1605.

[81] J. M. Frost, *Phys. Rev. B* **2017**, *96*, 195202.

[82] W. Rehman, R. L. Milot, G. E. Eperon, C. Wehrenfennig, J. L. Boland, H. J. Snaith, M. B. Johnston, L. M. Herz, *Adv. Mater.* **2015**, *27*, 7938.

[83] N. F. Mott, *Proc. Phys. Soc., London, Sect. A* **1949**, *62*, 416.

[84] P. Y. Yu, M. Cardona, *Fundamentals of Semiconductors: Physics and Materials Properties*, Springer, London **2010**.

[85] Z. Chen, C. L. Yu, K. Shum, J. J. Wang, W. Pfenninger, N. Vockic, J. Midgley, J. T. Kenney, *J. Lumin.* **2012**, *132*, 345.

[86] G. E. Eperon, S. D. Stranks, C. Menelaou, M. B. Johnston, L. M. Herz, H. J. Snaith, *Energy Environ. Sci.* **2014**, *7*, 982.

[87] S. B. Nam, D. C. Reynolds, C. W. Litton, R. J. Almassy, T. C. Collins, C. M. Wolfe, *Phys. Rev. B* **1976**, *13*, 761.

[88] *Semiconductors—Basic Data*, Springer, Berlin **1996**.

[89] T. Seifert, S. Jaiswal, M. Sajadi, G. Jakob, S. Winnerl, M. Wolf, M. Klaui, T. Kampfrath, *Appl. Phys. Lett.* **2017**, *110*, 252402.

[90] T. Seifert, S. Jaiswal, U. Martens, J. Hannegan, L. Braun, P. Maldonado, F. Freimuth, A. Kronenberg, J. Henrizi, I. Radu, E. Beaurepaire, Y. Mokrousov, P. M. Oppeneer, M. Jourdan, G. Jakob, D. Turchinovich, L. M. Hayden, M. Wolf, M. Munzenberg, M. Klaui, T. Kampfrath, *Nat. Photonics* **2016**, *10*, 483.

1804506 (10 of 10)